Astron. Astrophys. 325, 1226–1236 (1997)

ASTRONOMY
AND
ASTROPHYSICS

Thermal physics of asteroids

III. Irregular shapes and albedo variegations

Johan S.V. Lagerros⋆

Uppsala Astronomical Observatory, Box 515, S-751 20 Uppsala, Sweden

Received 21 January 1997 / Accepted 24 March 1997

Abstract. A new thermophysical model for asteroids is described, which allows for (almost) arbitrary shapes, albedo variegations, beaming, and heat conduction. Multiple scattering is considered in both the visual and the infrared wavelength region. The computational efforts are reduced to acceptable levels by using view factor algebra for the multiple scattering, and an iterative method for solving the heat conduction equation. This enables a statistical investigation, here using a set of Gaussian random shapes, spanning a range of various geometries. The model is also applied to the asteroids 243 Ida, 951 Gaspra, 4179 Toutatis, 4769 Castalia, and the moons of Mars, Phobos and Deimos, where shapes are known from radar measurements or direct imaging.

The self heating parameter is introduced in order to measure the degree of concavity of a given shape. The self heatings of the five objects with known shapes are rather low, which means that only a small portion of the radiation energy participates in the multiple scattering process on larger scales. In relation to the thermal beaming, the self heating on small scales is computed for a few surface roughness models, and is found to be substantially larger.

Thermal and visual light curves for the synthetic shapes are compared to each other, as well as to the curves produced by fitted ellipsoids. The differences between the models can be substantial, and in general becomes more pronounced at shorter wavelengths. There are systematic trends with increasing self heating, but the interpretation is that this is due to the increased asymmetry rather than the concavities themselves playing an important role.

A statistical test to detect albedo variegations is proposed, based on the comparison between thermal and visual light curves. The sensitivity of the test is investigated over a wide range of shapes and albedo patterns. The probability of detecting albedo spots is the highest at wavelengths close to the emission peak.

Key words: asteroids – radiation mechanisms: thermal – infrared: solar system – conduction

⋆ Johan.Lagerros@astro.uu.se

1. Introduction

Fundamental to the study of the physical properties of asteroids are their sizes and geometrical figures. Ground based lightcurve data indicate that many asteroids are highly elongated. The Galileo images of 243 Ida and 951 Gaspra (Belton et al. 1992; Belton et al. 1996), and the radar images of for example 4179 Toutatis and 4769 Castalia (Ostro et al. 1995; Hudson & Ostro 1994), reveals asymmetric bodies with complex topographies. The question is what the shapes and sizes of asteroids tells us about their collisional history, distributions in mass, density and composition throughout the various populations.

So far, only a very small fraction of the total population can be reached by detailed radar studies or direct imaging. The vast majority has to be studied using more indirect methods. Low order estimates on sizes and shapes have been derived using radiometric methods (Lebofsky & Spencer 1989) and lightcurve inversion methods (Magnusson et al. 1989). The meaning of low order is that we can only expect to derive very rough estimates on the geometrical figure from ground based light curve data. This is due to the intrinsic problems in the process of trying to invert 1-dimensional data (in time) into a 3-D shape with possible albedo variegations.

The radiometric methods are based on the comparison between reflected visual radiation and thermal infrared emission, to determine the total energy budget and thereby the size. From this point of view, the complex asteroidal shapes are causing some difficulties. The thermal models so far have assumed highly idealized shapes; spheres in the Standard Thermal Model (STM) (Morrison 1977; Morrison & Lebofsky 1979; Lebofsky et al. 1986; Lebofsky & Spencer 1989) or ellipsoids (Brown 1985; Lagerros 1996a). To these smooth bodies, effects of macroscopical surfaces roughness is added. That is, roughness on scales larger than millimeters but still far below the global scale. The ranges of scales in between have not been investigated so far. This is understandable given the complexity of the problem, not only in terms of deriving a working model describing the effects of multiple scattering within concavities, mutual heating, heat conduction, etc. Also, there is the nontriv-

ial problem of describing and generating ensembles of shapes, representing true asteroidal shapes.

Other than the shape, there is also the possibility of albedo variegations on the surface. From visual data alone there are intrinsic uniqness problems in determining if the light curve is caused by the shape or by albedo patterns. A comparison between the visual and thermal IR could be a solution, since a dark spot in the visual would be hot in the IR due to the higher absorption, and vice versa. This test has for example been applied, with negative result, to 45 Eugenia and 532 Herculina (Lebofsky et al. 1988), for which albedo spots were suspected (Taylor et al. 1987; Taylor et al. 1988). So far shape effects and spots have been treated separately. The question is how these effects interacts, and to what degree they might be confused.

Thus there is a need to improve our current thermophysical models of asteroids. Not only to obtain better diameters, but also to use the thermal infrared to get information on the composition, surface texture, regolith properties, and albedo patterns. Furthermore, several new far infrared instruments are going to use asteroids as calibrators, since they cover the large dynamical range in fluxes between stars and planets.

This is the third paper in a series concerning the improvement of the thermal models of asteroids. The model described in Paper I (Lagerros 1996a), included ellipsoidal shapes, heat conduction, and beaming. This was extended to the microwave regime in Paper II (Lagerros 1996b), to study the possibility of polarized emission. Here the modeling is taken further by allowing for almost arbitrary shapes and albedo patterns. Multiple scattering between facing surface elements is taken into account, both in the visual and in the thermal infrared. The model is used in order to study the effects of complex shapes and albedo variegations. Since the true shape is known only for very few asteroids, a set of Gaussian random shapes were generated (Muinonen 1996a). The model is then tested for a range from very smooth to rather irregular shapes. Albedo variegations are added in order to investigate the difficulties in using thermal data in order to detect spots on irregular asteroids.

2. Theory

The geometrical part of the model first concerns the generation of random shapes, characterized by only two parameters. For a non-convex body, shadows and internal visibility has to be considered, using geometrical optics. Multiple scattering between facing parts of the surface is handled by view factor algebra.

In the thermophysical part, each facet is heated by the Sun and scattered visual and thermal radiation from neighbouring facets. The heat conduction problem is, however, considered to be local within the facets, since the lateral extent of the facets is more than a factor 10^6 larger than the penetration depth of the diurnal heat wave. Multiple scattering and heat conduction is considered simultaneously. If the shape model is detailed enough, large craters are modelled within this framework. Roughness below the resolution of the shape model is treated statistically, by applying a correction to the radiation field from the smooth facet. The final step is to produce synthetic visual and thermal light curves from the disk integrated flux.

2.1. Gaussian random shapes

The constraints of the model are that the surface has to be mathematically "star-shaped", and it should be possible to define surface normals. That is, the surface can be described by a differentiable function $\boldsymbol{r} = \boldsymbol{r}(\theta, \phi)$, in spherical coordinates. There are several different possibilities to obtain model shapes $\boldsymbol{r}(\theta, \phi)$. Here, however, Gaussian random particles are generated, following the approach by Muinonen et al. (Muinonen 1996a, 1996b; Muinonen et al. 1996).

Consider a set of N random variables $\boldsymbol{s} = (s_1, \ldots, s_N)^{\mathrm{t}}$ for given spherical coordinates $\boldsymbol{\Omega} = (\phi_1, \theta_1; \ldots; \phi_N, \theta_N)$. The random variables are assumed to obey multivariate lognormal statistics, with zero means, such that the probability density for the shape is

$$p_N(\boldsymbol{s}, \Sigma_s) = \frac{1}{(2\pi)^{N/2}\sqrt{\det \Sigma_s}} \exp\left(-\frac{1}{2}\boldsymbol{s}^{\mathrm{t}}\Sigma_s^{-1}\boldsymbol{s}\right),$$

where Σ_s is the $N \times N$ covariance matrix. The vector $\boldsymbol{s}$ contains N logarithmic radii (or "logradii") which are related to the radii $(r_1, \ldots, r_N)$, by $s_i = \beta^2/2 + \ln(r_i/a)$. The radii have the mean a and variance $\sigma^2 = \exp\beta^2 - 1$. The covariance matrix elements are given by the autocorrelation function $C_s = C_s(\gamma)$, such that $\Sigma_{s,ij} = \beta^2 C_s(\gamma_{ij})$, where γ_{ij} is the angular distance between the directions i and j.

Gaussian random shapes can be generated by expanding the logradius and the autocorrelation function into spherical harmonics and Legendre polynomials, respectively. If, for degree l and order m, $P_l^m(x)$ is the associated Legendre function and $P_l(x)$ the Legendre polynomial, the shape is described by

$$\begin{aligned}
\boldsymbol{r}(\theta, \phi) &= (r\cos\phi\sin\theta, r\sin\phi\sin\theta, r\cos\phi) \\
r(\theta, \phi) &= \frac{a}{\sqrt{1+\sigma^2}} \exp s(\theta, \phi), \\
s(\theta, \phi) &= \sum_{l=0}^{\infty}\sum_{m=0}^{l} P_l^m(\cos\theta)(a_{lm}\cos m\phi + b_{lm}\sin m\phi), \\
C_s(\gamma) &= \sum_{l=0}^{\infty} c_l P_l(\cos\gamma),
\end{aligned}$$

where the coefficients a_{lm} and b_{lm} are independent Gaussian random variables with zero means and equal variances

$$\beta_{lm}^2 = (2 - \delta_{m0})\frac{(l-m)!}{(l+m)!}c_l\beta^2$$

There are several possibilities for the correlation function. The constraints are that $C_s(0) = 1$, $C_s'(0) = 0$, and $C_s(\gamma) = C_s(\gamma + 2\pi)$. The function used here is

$$C_s(\gamma) = \exp\left(-\frac{1}{2}\frac{\sin^2\gamma/2}{\sin^2\Gamma/2}\right),$$

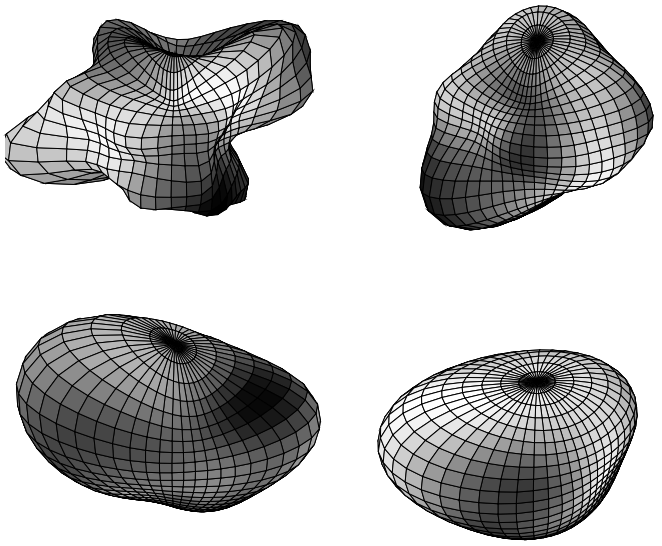

Fig. 1. Examples of shapes generated. In this figure $\sigma = 0.3$, and from the top, left to right, $\Gamma = 20^\circ$, 35°, 50°, and 65°. The global self heatings (Eq. 5) for these shapes are $\chi = 0.08$, 0.004, $3 \cdot 10^{-4}$, and 10^{-7}, respectively. Albedo patterns have been drawn using $\Gamma = 30^\circ$.

where Γ is the correlation angle. With this choice, the coefficients in the Legendre expansion becomes

$$c_l = (2l + 1) \exp(-\kappa) i_l(\kappa) \qquad l = 0, \ldots, \infty$$

where $\kappa = [4 \sin^2(\Gamma/2)]^{-1}$, and i_l the modified spherical Bessel function.

Thus the parameters determining the shape are σ and Γ. Increasing the variance σ^2 will simply increase the "roughness" of the shape (standard deviation in r), while increasing Γ will cause longer distances between hills and valleys on the surface. This is illustrated in Fig. 1.

It is also convenient to use the multivariate statistics to describe albedo and/or emissivity patterns on the surface. This can be achieved by defining

$$A_{\rm L}(\theta, \phi) = s(\theta, \phi) + \langle A_{\rm L} \rangle \tag{1}$$

The resulting albedo pattern has a mean $\langle A_{\rm L} \rangle$, standard deviation β, and correlation angle Γ between the spots. To ensure that the albedos are within the allowed range $0 < A_{\rm L} < 1$, a cut off may have to be applied a few standard deviations β below and above $\langle A_{\rm L} \rangle$.

2.2. Shadows

For a convex body, there are no internal shadows, and whether a given point on the surface is sunlit or not, is trivially determined by the zenith angle. If, on the other hand, there are concavities there will be mutual energy exchange between facing surface elements, as well as internal shadows to consider. The procedure is to first check for tilt shadows (zenith angle $\geq 90^\circ$), and after that projected shadows, which occurs when parts of the surface blocks the line of sight.

It is useful to define the visibility function to be $v_{ij} = 1$ if there is nothing obstructing the path from facet i to j, and $v_{ij} = 0$ if there are any tilt or projected shadows. For the purposes of this paper, the visibility function is derived using two different methods. The first method is used when calculating the intra-facet visibility. Consider the connecting line between two points i to j on the surface. If, for any point (r_p, θ_p, ϕ_p) on the connecting line: $r_p \leq r(\theta_p, \phi_p)$, the path is obstructed and $v_{ij} = 0$.

The intra-facet method is also possible to use when one point is outside the surface (the Sun or the observer). Interpolating r in the (θ, ϕ)-grid is, however, time consuming. A more efficient way is to compute the local horizon at every point on the surface. The local horizon is divided into a number of azimuth intervals, and the zenith distance to the horizon, in each interval, is stored in a lookup table. The visibility function is then calculated by simply looking up the correct azimuth interval and check that the zenith distance is small enough for the object to be above the local horizon. Computing the local horizon for every facet is time consuming, but is a one-time job for each surface.

2.3. View factors

The problem of multiple scattering is here treated by the use of radiosity matrix methods, following the approach by Özişik (1985). View factors are defined as the fraction of radiative energy from one surface facet directly hitting another facet. Thus for a surface built up by N facets there are N^2 view factors to consider. Most of them are, however, zero due to tilt and projected shadows. Also, the view factor from one facet to itself is here defined to be zero.

Assuming for simplicity that the facets are small, planar and that Lambert's law of reflection holds, the view factor going from facet i to j is

$$F_{ij} = v_{ij} \frac{\cos\theta_i \cos\theta_j}{\pi r^2} s_j$$

where, s_i the area of facet i, r the distance between the facets and θ_i the angle between the normal of facet i and the line connecting the two facets. From this definition, the reciprocity relation follows immediately:

$$s_i F_{ij} = s_j F_{ji}$$

The radiosity J_i is defined as the total radiation flux reflected and emitted from facet i, while the irradiation G_i is the flux incident on the facet. Using view factors the irradiation can be expressed as the sum of the contributions from the surrounding facets

$$G_i = \sum_{j \neq i} G_{j \to i} = \frac{1}{s_i} \sum_{j \neq i} J_j s_j F_{ji} = \sum_{j \neq i} F_{ij} J_j$$

Assume for simplicity that the spectrum can be divided into two parts, where the facets are heated by the Sun at visual wavelengths (V) whereas in the infrared region (IR) the radiation is dominated by the thermal emission. The absorptivity in the two

bands are denoted $\alpha_{\rm V}$ and $\alpha_{\rm IR}$, and by Kirchhoff's law they equal the emissivities $\varepsilon_{\rm V}$ and $\varepsilon_{\rm IR}$, respectively. If $r_{\rm h}$ is the directional-hemispherical reflectance, $\alpha = 1 - r_{\rm h}$. For a Lambert surface $r_{\rm h}$ equals the Lambert law albedo $A_{\rm L}$.

The radiosity is then given by the reflected irradiation and the thermal emission, such that

$$\begin{aligned} J_{{\rm V},i} &= (1-\alpha_{{\rm V},i})G_{{\rm V},i} \\ J_{{\rm IR},i} &= (1-\alpha_{{\rm IR},i})G_{{\rm IR},i} + \varepsilon_{{\rm IR},i}\sigma T_i^4 \end{aligned}$$

in which T_i is the surface temperature of facet i. By using the view factors, the irradiation in the two bands can be expressed as

$$\begin{aligned} G_{{\rm V},i} &= \sum_{j\neq i} F_{ij} J_{{\rm V},j} + \frac{S_\odot}{r^2}\mu_i \\ G_{{\rm IR},i} &= \sum_{j\neq i} F_{ij} J_{{\rm IR},j} \end{aligned}$$

where $S_\odot/r^2$ is the solar constant at a distance r (in AU) from the Sun, and μ_i cosine of the angle between normal of the facet and the direction to the Sun. The $\mu_i = 0$ if the Sun is not visible to the facet. This immediately leads to the elimination of the irradiation, and results into two systems if linear equations

$$\frac{1}{1-\alpha_{{\rm V},i}} J_{{\rm V},i} - \sum_{j\neq i} F_{ij} J_{{\rm V},j} = \frac{S_\odot}{r^2}\mu_i \tag{2}$$

$$\frac{1}{1-\varepsilon_{{\rm IR},i}} J_{{\rm IR},i} - \sum_{j\neq i} F_{ij} J_{{\rm IR},j} = \frac{\varepsilon_{{\rm IR},i}}{1-\varepsilon_{{\rm IR},i}}\sigma T_i^4 \tag{3}$$

The relation between these two systems is given by the net flow of heat into the surface

$$\begin{aligned} q_i &= G_i - J_i = (G_i - J_i)_{\rm V} + (G_i - J_i)_{\rm IR} \\ &= \frac{\alpha_{{\rm V},i}}{1-\alpha_{{\rm V},i}} J_{{\rm V},i} + \frac{\varepsilon_{{\rm IR},i}}{1-\varepsilon_{{\rm IR},i}}\left(J_{{\rm IR},i} - \sigma T_i^4\right). \end{aligned} \tag{4}$$

This equation is then part of the heat conduction problem, transporting energy between the immediate surface and the material below.

2.4. The self heating

Later on we will need to give a measure on the roughness of the shapes generated as described above. This is of course done in a way by the correlation angle Γ and the variance σ^2. Of interest here is, however, the effects of introducing concavities in the model, and Γ and σ does not give a direct measure of that. Therefore, the "degree of concavity" is here measured by the *self heating parameter* χ, which is defined as the ratio between the power directly striking the surface itself to the total power emitted from the surface, when kept isothermal. In other words, if the radiosity is the same for every facet $J_i = J$,

$$\chi = \frac{\sum_i G_i s_i}{\sum_i J s_i} = \frac{\sum_i \sum_{j\neq i} F_{ij} s_i}{\sum_i s_i} \tag{5}$$

Thus χ is a purely geometrical quantity, which is zero for a convex body, and equals unity inside for example a spherical shell.

Roughly speaking the self heating compares the surface area to the area of the convex hull (with some correction). The latter area is finite, while in reality the former is almost infinite. Thus, in principle, the self heating is always close to unity for the rough, cratered, and fractured asteroids. The meaning of this is simply that radiative transfer is important at some scales. The important discussion here is the contribution from each scale to the self heating. Thus the *global* self heating is given for some rough solar system objects in Table 1.

The thermal beaming is believed to be caused by the small scale self heating. In Sect. 4 the small scale self heating is derived for a few surface roughness models.

2.5. The heat conduction problem

In the one-dimensional heat conduction problem, the heat flow into a facet i is

$$q_i = -\kappa \left.\frac{\partial T_i}{\partial z}\right|_{z=0}, \tag{6}$$

where z is the depth, and κ is the thermal conductivity. Within the surface the heat flow is controlled by the heat diffusion equation

$$\rho c \frac{\partial T_i}{\partial t} = \kappa \frac{\partial^2 T_i}{\partial z^2}$$

It is very convenient to make a transformation into dimensionless variables. Following Paper I, this is achieved by

$$\begin{aligned} t' &= \omega t \qquad \text{where } 2\pi/\omega \text{ is the rotational period} \\ z' &= z/l_{\rm s} \qquad l_{\rm s} = \sqrt{\kappa/\rho c\omega} \\ u_i &= T/T_{{\rm ss},i} \qquad T_{{\rm ss},i}^4 = \alpha_{{\rm V},i} S_\odot/\varepsilon_{{\rm IR},i}\sigma r^2 \\ G_i' &= G_i \cdot r^2/S_\odot \\ J_i' &= J_i \cdot r^2/S_\odot \end{aligned}$$

together with the thermal parameter

$$\Theta_i = \frac{\sqrt{\kappa\rho c}\sqrt{\omega}}{\varepsilon_{{\rm IR},i}\sigma T_{{\rm ss},i}^3}$$

The radiosity Eqs. (2) and (3), are then transformed into

$$\frac{1}{1-\alpha_{{\rm V},i}} J'_{{\rm V},i} - \sum_{j\neq i} F_{ij} J'_{{\rm V},j} = \mu_i(t') \tag{7}$$

$$\frac{1}{1-\varepsilon_{{\rm IR},i}} J'_{{\rm IR},i} - \sum_{j\neq i} F_{ij} J'_{{\rm IR},j} = \frac{\alpha_{{\rm V},i}}{1-\varepsilon_{{\rm IR},i}} u_i^4(z'=0) \tag{8}$$

The heat conduction equation becomes

$$\frac{\partial u_i}{\partial t'} = \frac{\partial^2 u_i}{\partial z'^2}, \tag{9}$$

and the boundary condition at $z' = 0$, in Eqs. (4) and (6)

$$u_i^4 = \Theta_i \left.\frac{\partial u_i}{\partial z'}\right|_{z'=0} + \sum_{j\neq i} F_{ij}\left(J'_{\mathrm{V},j} + \frac{\varepsilon_{\mathrm{IR},i}}{\alpha_{\mathrm{V},i}} J'_{\mathrm{IR},j}\right) + \mu_i(t') \quad (10)$$

The multiple scattering problem in V and IR, and the heat conduction problem has then been transformed into Eqs. (7)–(10), which have to be solved simultaneously. Eq. (10) could be simplified somewhat using Eqs. (7) and (8), but the form used is more convenient when solving Eq. (10), as discussed in Sect. 4.

As desired, for a convex body, all $F_{ij} = 0$ and the equations degenerate to the model described in Paper I. Furthermore, assuming the convex body to be a sphere and $\Theta_i = 0$, we have in essence the Standard Thermal Model (STM). It is also of some practical interest to note that even for a very complex shape, a substantial fraction of the facets may have all their $F_{ij} = 0$, and can thus be treated separately, neglecting multiple scattering and thereby lowering the computational efforts.

The first step in finding a solution, is to solve Eq. (7) which is separated from the thermal physics and only depends on the geometry. The next step is then to iteratively solve the three remaining equations. If $\Theta = 0$ (but still some $F_{ij} \neq 0$), then Eq. (8) can be combined with Eq. (10) into the system of equations

$$J'_{\mathrm{IR},i} - \sum_{j\neq i} F_{ij} J'_{\mathrm{IR},j} = \frac{\alpha_{\mathrm{V},i}}{1-\alpha_{\mathrm{V},i}} J'_{\mathrm{V},i} \quad (11)$$

which together with Eq. (7) forms the slow rotator model. The fast rotator model ($\Theta \to \infty$) on the other hand implies that u_i is constant and $\partial u_i/\partial z' = 0$. The temperature is then controlled by the averaged solar insolation. Replacing μ_i, $J'_{\mathrm{V},i}$, and $J'_{\mathrm{IR},i}$ by their time averages, it is clear that Eqs. (7), (8) and (11) still holds, which yields the fast rotator temperature u_i.

2.6. The beaming

The beaming of the thermal emission in the solar direction is believed to be caused by the surface roughness. In Paper I the beaming was introduced as a correction function Λ to the Planck function $B_\lambda \to \Lambda B_\lambda$. The beaming function is a function of surface roughness, illumination and viewing geometry, temperature and wavelength. In Paper I the beaming function is derived by comparing a smooth surface to a surface filled by a fraction f of spherical segments with depth-to-diameter ratio S, such that

$$\Lambda = \Lambda(S, \alpha, \mu, \mu_\mathrm{e}, X, f)$$

where α is the phase angle, and $X = hc/\lambda k T_{\mathrm{SS}}$.

2.7. Disk integrated flux

When the equations of heat conduction and radiative transfer have been solved, the next step is to compute observable quantities. In this case the disk integrated flux, since asteroids in general are not disc resolved. In the two bands the approach is similar in the sense that the contribution from every facet in sight has to be added up, with some care taken for scattered light from surrounding facets. If $I_\lambda(\boldsymbol{r})$ is the intensity at a point $\boldsymbol{r}$ on the surface, the flux at a distance D is here approximated by

$$\begin{aligned} F_\lambda &= \frac{1}{D^2}\iint \mu_\mathrm{e} I_\lambda(\boldsymbol{r})\, ds \\ &= \frac{1}{D^2}\iint \mu_\mathrm{e} I_\lambda(\boldsymbol{r}) |\partial_\phi \boldsymbol{r} \times \partial_\theta \boldsymbol{r}|\, d\phi\, d\theta \\ &\approx \frac{1}{D^2}\sum_i w_i \mu_{\mathrm{e},i} I_\lambda(\phi_i, \theta_i) s_i, \end{aligned}$$

where $\mu_{\mathrm{e},i}$ is cosine of the angle between the direction to the observer and the normal of facet i, and w_i is added for the possibility to improve the estimate by the use of for example Simpson's rule.

The difference, however, between the infrared and the visual bands, is that in the latter there is no redistribution of energy between different wavelengths. That is, the contribution from facet i is proportional to $J'_{\mathrm{V},i}$. If S_λ is the solar spectral flux distribution, we have by multiplying with Eq. (7)

$$F_\lambda = \frac{S_\lambda}{D^2}\sum_i w_i \mu_{\mathrm{e},i} J'_{\mathrm{V},i} s_i$$

The thermal infrared is more complex since the radiation field is given non-linearly by the temperature derived above. The disk averaged IR intensity at a wavelength λ is given by adding up the blackbody emission from each facet, plus the reflected IR radiation from neighboring facets, such that

$$\begin{aligned} F_\lambda &= \frac{1}{D^2}\sum_i w_i \mu_{\mathrm{e},i} \times \\ &\quad \left(\varepsilon_{\mathrm{IR},i}\Lambda\frac{B_\lambda(T_i)}{\pi} + (1-\varepsilon_{\mathrm{IR},i})\sum_{j\neq i}\varepsilon_{\mathrm{IR},j} F_{ij}\frac{B_\lambda(T_j)}{\pi}\right) s_i \\ &= \frac{1}{\pi D^2}\sum_i w_i \mu_{\mathrm{e},i} s_i \times \\ &\quad \sum_j \big((1-\varepsilon_{\mathrm{IR},i})F_{ij} + \Lambda^2\delta_{ij}\big)\varepsilon_{\mathrm{IR},j} B_\lambda(T_j) \end{aligned} \quad (12)$$

where δ_{ij} is the Kronecker delta. Here, as an approximation, the beaming is only applied to the direct component.

Again it is convenient to introduce the dimensionless parameter $X_i = hc/\lambda k T_{\mathrm{SS},i}$, such that the Planck function can then be written $B_{\lambda,i} \propto 1/[\exp(X_i/u_i) - 1]$. From Wien's displacement law, the black body peak occurs at $X = 4.97$ in wavelength space, and at $X = 2.82$ in frequency space.

2.8. Detecting albedo variegations

In the "school book example", albedo spots on a perfect sphere are detected by the phase shift between the visual and thermal light curves. This test is, however, not easy to apply for more realistic shapes; at some point there will be a competition between the shape and the albedo pattern, and the definition of phase shifts becomes unclear since the shapes of the curves

Table 1. The degree of global self heating χ, as defined in Eq. (5), for some solar system objects.

Object	χ
243 Ida	0.012
951 Gaspra	0.0020
4179 Toutatis	0.0098
4769 Castalia	0.011
Phobos	0.0011
Deimos	0.0024

differs. Therefore, the following statistical test is proposed: if $f/\langle f\rangle$ is the observed normalized flux, it is likely that there are spots on the surface if

$$\max_t \left| \frac{f_{\rm V}(t)/\langle f_{\rm V}(t)\rangle}{f_{\rm IR}(t)/\langle f_{\rm IR}(t)\rangle} - 1 \right| > a \qquad (13)$$

where t is taken over one rotational period, and a is the cut off parameter. Even if there are no spots, the two curves will not be in perfect agreement, thus in general the cut off has to be $a > 0$. For a specific object, a could be derived by first using the light curve data to put some constraints on the possible shape. Within those limits a set of possible shapes should considered. For each hypothetical shape, light curves without spots are generated, and the LHS of Eq. (13) computed. The cut off a is then chosen so that the test falsely detects spots for a small prescribed fraction of the cases. Thereby there is a high probability that there are spots if the observed value is higher than the cut off. If it is lower, a conclusion is difficult to draw without the risk of making a confusion.

3. Results

A number of shapes were generated and geometrically analyzed, by using the methods described above. Synthetic visual and thermal light curves were generated for those shapes as well as for true asteroidal shapes. The light curves were compared to curves of ellipsoids, in order to investigate the effects of including concavities in the model.

3.1. Implementation

The model presented here was implemented mostly in MATLAB. The synthetic shapes were described using a (θ, ϕ)-grid consisting of $23 \times 44 = 1012$ grid points. The geometrical part, when computing the view factors and the local horizon, turned out to be the most time consuming. That part of the code could benefit the most from being rewritten in for example C/C++, or FORTRAN. The important point is, however, that the geometrical computations are only a one time job for a given shape.

The thermophysical part would on the other hand gain little from being rewritten. The matrices involved are quite large (1012×1012), but diagonal dominant and sparse; typically only a few percent of the elements are non-zero. The matrix equations were therefore solved using direct methods in MATLAB, within a few seconds on a Sun Sparc-station 20.

3.2. Real objects

Based on the Galileo images of the asteroids 243 Ida and 951 Gaspra, the Viking orbiter images of Phobos and Deimos, and radar mapping of 4179 Toutatis and 4769 Castalia, it has been possible to derive the 3-D shape of these bodies (Thomas 1989; Thomas et al. 1994; Thomas et al. 1996; Hudson & Ostro 1994; Hudson & Ostro 1995). The shape models were provided in various formats by P. Thomas and S. Hudson (private communications). The global self heatings calculated for these shapes are given in Table 1. Care should be taken when comparing these values, since the shape models differs in resolution and reliability at different locations on the surfaces. Nevertheless, the rather low values indicates that typically only a minor portion of the radiation participates in the multiple scattering process.

As an example, thermal light curves were generated for October 1, 1995 of 951 Gaspra at a wavelength $\lambda = 10\ \mu$m (Fig 2). The physical parameters used (shape, spin vector, albedo, etc) were taken from the results of the Galileo encounter (Davies et al. 1994; Thomas et al. 1994; Helfenstein et al. 1994). For comparison, curves were also computed using the ellipsoidal shape fitted to the true shape. The date was chosen to illustrate a situation where the ellipsoidal model would substantially differ from the true shape model. The ellipsoidal model produces perfectly symmetric curves, with higher fluxes, but lower amplitudes. On the other hand, at other aspect geometries the agreement between the two models can be in almost perfect agreement.

Beaming was applied to the models in Fig. 2, using the model described in Paper I. Qualitatively the only change of importance is the increase in flux.

3.3. Comparison with the ellipsoid

A set of 195 shapes were generated with parameters in ranges $\Gamma = 10°$–$90°$, and $\sigma = 0.05$–0.5. A few examples are shown in Fig. 1. For each shape, the view factors, local horizons, and the self heatings were calculated. Also, the center of mass and the inertia tensor were derived, assuming homogeneous bodies. In what follows the bodies were always rotated along the principal component with largest inertia.

It is of interest to compare the model of this paper, with for example the ellipsoids used in Paper I. This was achieved by, for each irregular shape, derive the ellipsoid with equal inertia tensor (implies equal orientation). By this choice, the fitted ellipsoid will dynamically behave the same way. The ellipsoids are described by their axis ratios a/b and b/c, where $a \geq b \geq c > 0$.

The generated shapes spans a wide range in self heating, $0 \leq \chi < 0.11$, with some bias towards $\chi = 0$. The axis ratios a/b and b/c of the equal inertia ellipsoids, both covers the interval 1–2, but with some preference towards spherical shapes.

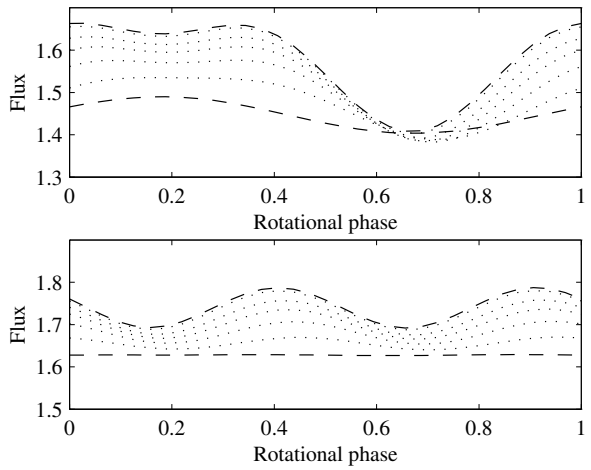

Fig. 2. Thermal light curves at $\lambda = 10\,\mu$m of 951 Gaspra, using the true shape (upper panel) and a fitted ellipsoid (lower panel). The amplitude decreases with increasing thermal parameter from $\Theta = 0$ (dashed line), 0.5, 1, 2, 5, to $\Theta = \infty$.

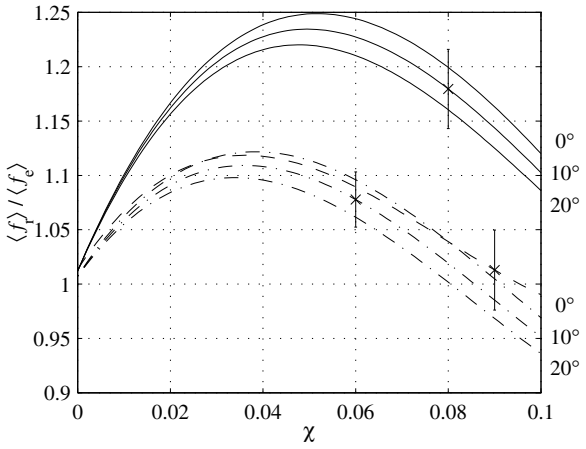

Fig. 3. The ratio between light curve mean fluxes for rough shapes and fitted ellipsoids. The comparisons are made for thermal light curves assuming $\Theta = 0$ (solid lines), $\Theta = \infty$ (dashed), and visual curves (dot-dash). The light curves were computed for phase angles $\alpha = 0°$, $10°$, and $20°$. The errorbars indicates the typical scatter around the third degree polynomials fitted to the computed data. The spin vectors were assumed to be perpendicular to the line of sight.

Thermal and visual light curves where generated for these bodies at phase angles in the range 0°–20°. The curves were generated under the two assumptions that $\Theta = 0$ (slow rotator) and $\Theta = \infty$ (fast rotator). The thermal beaming was excluded ($\Lambda \equiv 1$). The X parameter was taken to be $X = 8$, since when observing main belt asteroids with an albedo ~ 0.10 in the range $\lambda \sim 6$–$12\,\mu$m, $X \sim 5$–10. In general, the effects described here increases with X. There are also some changes in the shape of the light curves with increasing X, but they are small and are not further discussed here.

In Fig. 3 the predicted mean visual and IR fluxes of the rough model and the ellipsoidal model are compared, at different phase angles. To ease the comparison, third degree polynomials have been fitted to the computed ratios. Below self heatings $\sim 10\,\%$, both the visual and thermal fluxes are underestimated by the ellipsoidal model. With increasing phase angles the underestimate becomes less pronounced in the slow rotator case, while the fast rotator case is not affected.

In practical applications – for example diameter determinations – the observed visual and thermal IR fluxes are compared. Both fluxes are proportional to the projected area seen by the observer, which means that one might consider a thermal model as something which prescribes a ratio between the two fluxes. In Fig. 4 the ratio between the mean IR and visual fluxes are plotted. The physical properties are the same except for the shape. Since the effects of the projected area are removed by the division, the diagram illustrates the result of different slope and temperature distributions. Already at $\chi = 0$ there is a 5 % scatter around the normalization point. With higher self heatings there is a systematic trend to expect higher IR fluxes, compared to what a convex model would produce. At higher phase angles the trend in the slow rotator case gradually comes closer to the fast rotator case.

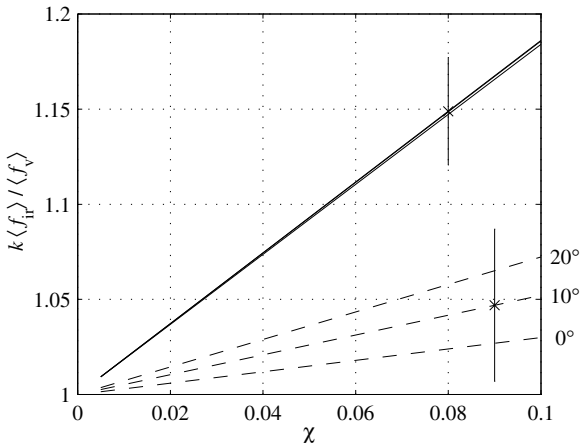

Fig. 4. The ratio between mean IR and visual fluxes, for $\Theta = 0$ (solid line) and $\Theta = \infty$ (dashed). Computed for phase angles $\alpha = 0°$, $10°$, and $20°$, and the spin vector perpendicular to the line of sight. The normalization factors k used for the two cases, are chosen to facilitate the comparison. The errorbars indicates the typical scatter around the lines fitted to the computed data.

3.4. Albedo spots

The possibility to detect albedo variegation on irregular objects was tested using the method described in Sect. 2.8. As an example, the 195 random shapes from the previous section was used again. This fictitious asteroid population is not without biases, but since it spans a wide range of shapes it should give a lower bound on the abilities of the detection method.

In all cases, the mean albedo was taken to be $\langle A_{\rm L} \rangle = 0.2$, heat conduction was neglected, the objects assumed to be at opposition with the spin vector perpendicular to the line of sight. The thermal light curves were computed for a range of wavelengths, in the range described by $2 \leq \langle X \rangle \leq 12$. First the

Table 2. The cut-off parameter in Eq. (13). See text for details.

X	a	X	a
2	0.076	8	0.205
3	0.024	9	0.241
4	0.041	10	0.271
5	0.087	11	0.301
6	0.126	12	0.325
7	0.166		

cut off was computed by making the test falsely detect spots on the surfaces with constant $A_{\rm L} = 0.2$, in 5 % of the cases (see Table 2). Different types of random albedo patterns were generated using Eq. (1), described by $0.02 \leq \beta \leq 0.06$, and $20^\circ \leq \Gamma \leq 150^\circ$. These fairly large albedo contrasts where chosen in order to illustrate the general principles. For a given shape and pattern type (β, Γ), light curves were computed using 10 different random albedo maps. For each pair of visual and thermal light curves, the test was applied and the success rate recorded. Since the test would not be applied to observational data with too small amplitudes, curves were excluded from the statistics if their amplitudes were less than 5 %,

A total of about 300 000 thermal and visual curves were produced and analyzed. The probability to detect albedo variegations for different types of patterns and at different wavelengths is shown in Figs. 5 and 6. As expected the contrast is more important than the typical distribution. At the configuration used here, it is easier to detect spots close to the equator. The drop of in detection probability with increasing Γ can be explained by the higher probability for the spots to appear only in the polar regions. At small enough Γ on the other hand, the number of spots seen by the observer at any given time is more or less constant.

The increased probability to detect spots close to the emission peak can be understood by the tighter a-constraint in Eq. (13). The cut off is the smallest at wavelengths where absorption-reemission process is the closest to the reflection process, enabling a safe detection. At short wavelengths the emission is temperature sensitive in a highly non-linear way. At longer wavelengths the emission becomes $f_{\rm IR} \propto \mu_{\rm e} T \propto \mu_{\rm e} \mu^{1/4}$, which should be compared to $f_{\rm V} \propto \mu_{\rm e} \mu$ for Lambert's law.

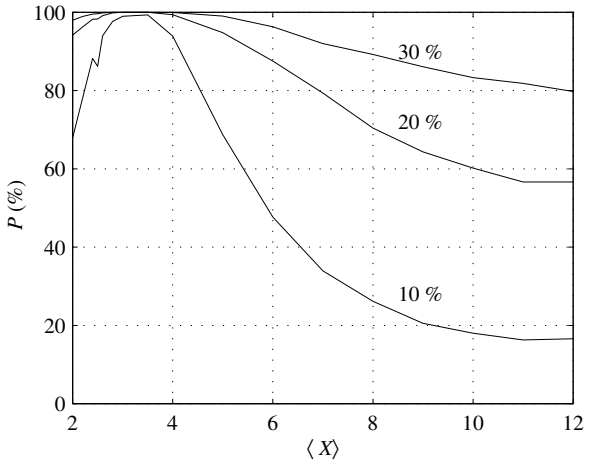

Fig. 5. The probability P to detect albedo spots at different wavelengths, described by $\langle X \rangle = \langle hc/\lambda k T_{{\rm SS},i} \rangle_i$. Curves are drawn for albedo contrasts $\beta/\langle A_{\rm L} \rangle$ = 10 %, 20 %, and 30 %. The correlation angle $\Gamma = 50^\circ$.

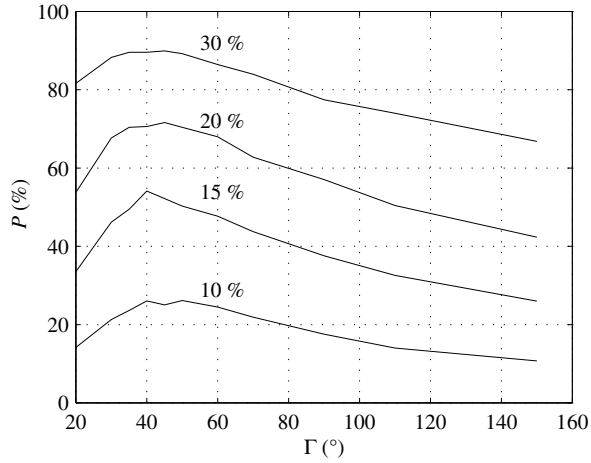

Fig. 6. The probability P to detect albedo spots at $\langle X \rangle = 8$, for different types of albedo patterns described by the correlation angle Γ. Curves are drawn for different albedo contrasts $\beta/\langle A_{\rm L} \rangle$ = 10 %, 15 %, 20 %, and 30 %.

4. Discussion

In conclusion, irregular shapes, albedo patterns, beaming, and heat conduction have been considered in the model presented here. By each physical process included, the complexity and number of unknown parameters increases rapidly. Therefore, the focus here has been placed on the effects caused by the irregular shape and albedo variegations. The aim has been to derive computationally efficient methods, in order to allow not only for models of single objects, but also for larger statistical investigations.

Comparing this model with the previous ellipsoidal model in Paper I, both the shape, and the absolute level of the thermal light curves might differ a lot, as illustrated in Fig. 2. For diameter determinations, the absolute level or mean flux is of more interest. The mean fluxes produced by the ellipsoids in Fig. 3 are systematically too small if major concavities are present. A more model independent approach would be to do a direct comparison between visual and IR, as simulated in Fig. 4. There are still systematic trends, but less pronounced, especially if one considers the low self heatings in Table 1, compared to the rather high values for some of the synthetic shapes. The general conclusion is that it appears to be important to model more complex shapes than ellipsoids, but not necessarily non-convex. This is understandable given the relatively low self heatings seen here;

multiple scattering within global scale concavities is probably of somewhat less importance.

With the aid of a fast enough model, it was possible to compute the large number of light curves needed in order to investigate the albedo variegation test proposed in Sect. 2.8. There are, of course, several possible alternatives to Eq. (13), but it proved to be more efficient than a few other methods tested. The results in Figs. 5 and 6 are rather model dependent, and are based on a highly idealize scenario. Nevertheless, the qualitative results are of general interest. If the observations take place close to the emission peak, even rather small differences in shape between the thermal and visual light curves can, with high probability, be interpreted as due to spots on the surface. This should be compared to other methods, for example measuring colour variations in the visual light curves. Even for a bright object, with significant albedo markings, such as 4 Vesta the colour variations are only a few percent (Reynoldson et al. 1993).

A wide range of shapes and albedo patterns have been described only by the correlation angle, and the standard deviation. The small number of parameters is not only convenient, but is also a necessity for statistical investigations, as exemplified above. The obvious question is then how close these synthetic shapes and albedo patterns are to the reality. Unfortunately there are only a few shapes available to do statistics on. Furthermore, even if a given shape is Gaussian, it is not trivial to go backwards and estimate which correlation function and variance have been used. The topic of followup papers will be to put better constrains on the Gaussian random asteroids, based on the currently available shapes. Albedo variegations, how they are best described, and if they are uncorrelated to the features of the shape or not, is an even more complex question for the future.

The use of Lambert law scattering is a major simplifications made in this model. From a technical point of view this has to do with the view factor approach adopted above. The method does not allow for a reflected beam of light to remember where it came from, that is, no specular component in the reflection. There are several possible solutions to this problem, either to use a more exact ray tracing method, or to separate the multiple and the single scattering components. The later approach is perhaps preferable, since the ray tracing methods tends to be very computational expensive compared to the view factor methods. On the other hand, the use of more complex scattering laws are motivated in the visual, but perhaps not in the currently less evolved thermal infrared. Another solution is, of course, to neglect multiple scattering completely, based on the low self heatings found here, as discussed above.

Although they are included in the model, beaming and heat conduction have not been the main issue. The beaming has only been introduced in Eq. (12), but should strictly speaking be included in the multiple scattering process as well. Given the relatively small self heatings derived, this approximation should not be of major concern. It is probably more important to improve the models on a much smaller scale. The beaming effect, as caused by the surface roughness have been studied in a number of different ways (Hansen 1977; Vogler et al. 1991; Johnson et al. 1993; Jämsä et al. 1993). Spencer (1990) included heat conduction, while Hapke (1996) recently studied heat conduction in connection with a radiative transfer in a porous medium. Since it has been shown that all three aspects are important and coupled, the preferred picture for the future would be to consider heat conduction and radiative transfer in a rough and porous regolith, at the same time.

Acknowledgements. I thank Karri Muinonen for support and comments, especially concerning the random Gaussian shapes, and Claes-Ingvar Lagerkvist and Per Magnusson for general advice. Dr. P. Thomas and Dr. S. Hudson are acknowledged for kindly providing the shape models of a few irregular solar system objects. I also thank Dr. L. A. Lebofsky for his review.

Appendix A

A.1. Solving the heat conduction problem

The solutions to the heat conduction problem in Eq. (9) can be written as Fourier series expansions (Paper I):

$$u(z',t') \;=\; U_0 + \sum_{n=1}^{\infty} U_n e^{-\sqrt{n/2}\,z'} \cos(nt' - \sqrt{n/2}\,z' + \epsilon_n) \qquad \text{(A1)}$$

The difficulty is, however, finding the Fourier coefficients U_n and ϵ_n, satisfying the boundary condition in Eq. (10). In Paper I, for the convex model, the Fourier coefficients where computed by a finite difference method. Another possibility is to derive the coefficients directly from the boundary condition. The first step is to define

$$\mu_i^{\rm c} = \sum_{j\neq i} F_{ij} \left(J'_{{\rm V},j} + \frac{\varepsilon_{{\rm IR},i}}{\alpha_{{\rm V},i}} J'_{{\rm IR},j} \right) + \mu_i(t')$$

This gives the boundary condition at $z' = 0$

$$u_i^4 = \Theta_i \left. \frac{\partial u_i}{\partial z'} \right|_{z'=0} + \mu_i^{\rm c}$$

where the $\mu_i^{\rm c}$ is considered to be a known function (from Eq. (11) or a previous iteration finding $J_{\rm IR}$).

If, for the sake of clearness, the index i is dropped, the algorithm is

1. Divide the time interval $t' \in [0, 2\pi]$ into 2^n time steps.
2. Assume some initial values for the surface temperature u_k at time steps $k = 0, \ldots, 2^n - 1$.
3. Iterate through steps 4–7.
4. Compute the Fourier expansion of u_k by using the Fast Fourier Transform (FFT).
5. Compute $\partial_{z'} u_k$ from the Fourier coefficients and Eq. (A1).
6. Compute $\Delta_k = u_k^4 - \Theta\, \partial_{z'} u_k - \mu_k^{\rm c}$, if all the Δ_k's are small enough we have a solution.
7. Compute $u_k \leftarrow u_k - \eta \Delta_k / 4u_k^3$, where η is a parameter discussed below.

The parameter $\eta > 0$, has to be chosen small enough to make the method stable and large enough to make it converge as fast as possible.

When u_i has been calculated in this way, it is possible to refine $J_{\rm IR}$ by Eq. (8). Typically it takes only 2–4 iterations between $J_{\rm IR}$ and u_i until a solution to the Eqs. (7)–(10) is found.

A.2. Self heating and beaming

There have been several attempts to model the beaming as being caused by the surface roughness (Hansen 1977; Spencer 1990; Jämsä et al. 1993; Vogler et al. 1991; Johnson et al. 1993). The general idea is to consider a planar surface and then add roughness to it. The power escaping the rough surface is proportional to the area of the planar surface $A_{\rm p}$, while the total energy output is proportional to the rough surface area $A_{\rm r}$. Thus, the self heating is given by

$$\chi = 1 - \frac{A_{\rm p}}{A_{\rm r}}$$

In Paper I, the surface roughness is modeled by a flat surface filled by a fraction f of spherical craters, with a depth-to-diameter ratio $S = h/2\rho$. The area of one spherical segment is $4\pi\rho^2 S$, while the flat area area enclosed by the crater rim is $4\pi\rho^2 S(1-S)$. After some algebra it follows that

$$\chi = 1 - \frac{1-S}{1+S(f-1)} = \frac{Sf}{1+S(f-1)}$$

Using the roughness parameters from Paper I ($S = 1/2$, $f = 80\,\%$), one gets for the small scale self heating $\chi = 0.44$.

A more general model is to describe the surface roughness by a distribution function

$$a'(\upsilon,\zeta)\sin\upsilon\,d\upsilon\,d\zeta,$$

where υ is the angle to the vertical, ζ the azimuth, and $a'\sin\upsilon$ the density of normals pointing in the (υ,ζ)-direction (Hapke 1993). It is common to assume that the distribution function is azimuth independent, and normalized such that $\int_0^{\pi/2} a'(\upsilon)\,d\upsilon = 1$. Following Paper II, the area of the planar surface is given by projecting the element $\sin\upsilon\,d\upsilon\,d\zeta$ onto the plane and integrate:

$$A_{\rm p} = \int_0^{2\pi} d\zeta \int_0^{\pi/2} a'(\upsilon)\cos\upsilon\sin\upsilon\,d\upsilon,$$

while the rough area is

$$A_{\rm r} = \int_0^{2\pi} d\zeta \int_0^{\pi/2} a'(\upsilon)\sin\upsilon\,d\upsilon.$$

By this the self heating becomes

$$\chi = \frac{\int_0^{\pi/2} a'(\upsilon)(1-\cos\upsilon)\sin\upsilon\,d\upsilon}{\int_0^{\pi/2} a'(\upsilon)\sin\upsilon\,d\upsilon} \qquad \text{(A2)}$$

One example of a' is the Gaussian distribution function

$$a'(\upsilon) = \frac{2\sec^2\upsilon}{\pi\tan^2\overline{\theta}}\exp\left(-\frac{\tan^2\upsilon}{\pi\tan^2\overline{\theta}}\right)$$

where $\overline{\theta}$ is the mean slope angle of the surface roughness (Hapke 1984). From Eq. (A2) the self heating for this distribution is

$$\chi = 1 - \frac{E_1(\cot^2\overline{\theta}/\pi)}{\pi\tan\overline{\theta}\ \mathrm{erfc}(\cot\overline{\theta}/\sqrt{\pi})}$$

in which $E_1(x) = \int_1^\infty \exp(-xt)/t\,dt$ is the exponential integral. Examples of self heatings for some slope angles $\overline{\theta}$ are, $\chi(10^\circ) = 0.04$, $\chi(20^\circ) = 0.13$, and $\chi(30^\circ) = 0.22$.

References

Belton, M. J. S., Chapman, C. R., Klaasen, K. P., Harch, A. P., Thomas, P. C., Veverka, J., McEwen, A. S., and Pappalardo, R. T., 1996, Icarus 120, 1

Belton, M. J. S., Veverka, J., Thomas, P., Helfenstein, P., Simonelli, D., Chapman, C., Davies, M. E., Greeley, R., Greenberg, R., and Head, J., 1992, Science 257, 1647

Brown, R. H., 1985, Icarus 64, 53

Davies, M. E., Colvin, T. R., Belton, M. J. S., Veverka, J., and Thomas, P. C., 1994, Icarus 107, 18

Hansen, O. L., 1977, Icarus 31, 456

Hapke, B., 1984, Icarus 59, 41

Hapke, B., 1993, Theory of Reflectance and Emittance Spectroscopy, Cambridge University Press

Hapke, B., 1996, J. Geophys. Res. 101, 16817

Helfenstein, P., Veverka, J., Thomas, P. C., Simonelli, D. P., Lee, P., Klaasen, K., Johnson, T. V., Breneman, H., Head, J. W., Murchie, S., Fanale, F., Robinson, M., Clark, B., Granahan, J., Garbeil, H., McEwen, A. S., Kirk, R. L., Davies, M., Neukum, G., Mottola, S., Wagner, R., Belton, M., Chapman, C., and Pilcher, C., 1994, Icarus 107, 37

Hudson, R. S. and Ostro, S. J., 1994, Science 263, 940

Hudson, R. S. and Ostro, S. J., 1995, Science 270, 84

Jämsä, S., Peltoniemi, J. I., and Lumme, K., 1993, A&A 271, 319

Johnson, P. E., Vogler, K. J., and Gardner, J. P., 1993, J. Geophys. Res. 98, 20825

Lagerros, J. S. V., 1996a, A&A 310, 1011

Lagerros, J. S. V., 1996b, A&A 315, 625

Lebofsky, L. A., Greenberg, R., Tedesco, E. F., and Veeder, G. J., 1988, Icarus 75, 518

Lebofsky, L. A. and Spencer, J. R., 1989, in R. P. Binzel, T. Gehrels, and M. S. Matthews (eds.), Asteroids II, pp 128–147, Arizona University Press

Lebofsky, L. A., Sykes, M. V., Tedesco, E. F., Veeder, G. J., Matson, D. L., Brown, R. H., Gradie, J. C., Feierberg, M. A., and Rudy, R. J., 1986, Icarus 68, 239

Magnusson, P., Barucci, M. A., Drummond, J. D., Lumme, K., Ostro, S. J., Surdej, J., Taylor, R. C., and Zappalà, V., 1989, in R. P. Binzel, T. Gehrels, and M. S. Matthews (eds.), Asteroids II, pp 66–97, The University of Arizona Press

Morrison, D., 1977, Icarus 31, 185

Morrison, D. and Lebofsky, L. A., 1979, in T. Gehrels (ed.), Asteroids, pp 184–205, Arizona University Press

Muinonen, K., 1996a, Earth, Moon, Planets 72, 339

Muinonen, K., 1996b, J. Quant. Spectrosc. Radiat. Transfer 55, 603
Muinonen, K., Nousiainen, T., Fast, P., Lumme, K., and Peltoniemi, J. I., 1996, J. Quant. Spectrosc. Radiat. Transfer 55, 577
Ostro, S. J., Hudson, R. S., Jurgens, R. F., Rosema, K. D., Campbell, D. B., Yeomans, D. K., Chandler, J. F., Giorgini, J. D., Winkler, R., Rose, R., Howard, S. D., Slade, M. A., Perillat, P., and Shapiro, I. I., 1995, Science 270, 80
Özişik, M., N., 1985, Heat Transfer, A Basic Approach, McGraw-Hill Publishing Company
Reynoldson, G., Thacker, P., Erikson, A., and Oja, T., 1993, Minor Planet Bull. 20, 11
Spencer, J. R., 1990, Icarus 83, 27
Taylor, R. C., Birch, P. V., Drummond, J., Pospieszalska-Surdej, A., and Surdej, J., 1987, Icarus 69, 354
Taylor, R. C., Birch, P. V., Pospieszalska-Surdej, A., and Surdej, J., 1988, Icarus 73, 314
Thomas, P. C., 1989, Icarus 77, 248
Thomas, P. C., Belton, M. J. S., Carcich, B., Chapman, C. R., Davies, M. E., Sullivan, R., and Veverka, J., 1996, Icarus 120, 20
Thomas, P. C., Veverka, J., Simonelli, D., Helfenstein, P., Carcich, B., Belton, M. J. S., Davies, M. E., and Chapman, C., 1994, Icarus 107, 23
Vogler, K. J., Johnson, P. E., and Shorthill, R. W., 1991, Icarus 92, 80

This article was processed by the author using Springer-Verlag LaTeX A&A style file *L-AA* version 3.